Applied Geochemistry 140 (2022) 105295

Contents lists available at ScienceDirect

Applied Geochemistry

journal homepage: www.elsevier.com/locate/apgeochem

# Lithium isotope behavior under extreme tropical weathering: A case study of basalts from the Hainan Island, South China

Yan-Wen Xiong [a,b], Hua-Wen Qi [a,*], Rui-Zhong Hu [a], Yi-Lin Xiao [c], Li-Yan Wei [a,b]

[a] State Key Laboratory of Ore Deposit Geochemistry, Institute of Geochemistry, Chinese Academy of Sciences, Guiyang, 550081, China
[b] University of Chinese Academy of Sciences, Beijing, 100049, China
[c] CAS Key Laboratory of Crust-Mantle Materials and Environments, School of Earth and Space Sciences, University of Science and Technology of China, Hefei, 230026, China

ARTICLE INFO

Editorial handling by Dr Romain Millot

*Keywords:*
Lithium isotopes
Fe–Mn oxides
Chemical weathering
Basalt
Hainan Island (South China)

ABSTRACT

Chemical weathering of silicate rocks (especially basalt) is an important sink of atmospheric carbon dioxide, and has an important impact on long-term carbon cycle and storage. Lithium (Li) isotopes have been regarded as a good tracer of chemical weathering, however, the behavior of Li isotopes in tropical settings is poorly understood. In this study, we studied the Li elemental and isotopic variation in the solid weathering products (soil and saprolite) from a highly-weathered (CIA ~100%) basalt weathering profile (>15 m thick, including soil, saprolite, semi-weathered rock and fresh basalt) on the tropical Hainan Island in South China. The weathering products have 1.99–58.1 ppm Li, mostly below the average fresh basalt value (4.6 ppm, n = 5). The $\delta^7$Li values (−14.3 to 8.9‰) of the solid weathering products exhibit complex stratigraphic variation across the weathering profile. The Li and Mn enrichments coincide spatially, with the Mn-rich samples having the highest Li content and lowest $\delta^7$Li value. Lithium is enriched in the semi-weathered basalt sample, but its $\delta^7$Li value (−2.7‰) is close to that of fresh basalts (0.7–5.3‰, avg. 3.0‰, n = 5). Strontium isotope data show that the weathering profile is affected by marine aerosol input, and the marine strontium may have been leached to the profile bottom or out of it under extreme weathering. Sequential extraction results indicate that Li in the soil, saprolites (lower part), and semi-weathered basalt occurs mainly in the residual phase, while Li in the saprolites (middle part) occurs largely in Fe–Mn oxides. We suggest that Li isotope fractionation in the upper, middle and lower parts of the profile was controlled by, respectively, marine aerosol input and secondary mineral leaching, dissolution/re-precipitation of Fe–Mn oxides, and neoformation of secondary minerals from heavy pore water. Our results show that the preferential light Li isotope uptake by Fe–Mn oxides may have been the main cause for the major Li isotope fractionation in the Wenchang weathering profile.

## 1. Introduction

Chemical weathering of silicate rocks forms a link that connects the atmospheric, lithospheric and hydrospheric geochemical systems, which controls the elemental/isotopic cycling and transport from the land surface to water bodies. Furthermore, as a major carbon dioxide ($CO_2$) sink, chemical weathering plays a critical role in regulating the long-term Earth climate (Nesbitt, 1979; Nesbitt et al., 1980; Gardner et al., 1981; Walker et al., 1981; Berner et al., 1983; Gaillardet et al., 1999; Dessert et al., 2003). In recent years, many non-traditional isotope systems (e.g., Mg, Fe, Cu, Si, K, Mo, Ge, Li, Zn, Ni, and Ba) have been increasingly studied to understand the weathering process (Dauphas et al., 2017; Elliott and Steele, 2017; Moynier et al., 2017; Pennisston-Dorland et al., 2017; Poitrasson, 2017; Qin and Wang, 2017; Teng, 2017).

Lithium (Li), a soluble alkali element, is mainly hosted in silicate (rather than carbonate) minerals (Kisakürek et al., 2005). Lithium has two stable isotopes ($^6$Li and $^7$Li), whose large mass difference can lead to significant (up to 60‰) isotope fractionation (Tomascak, 2004). Lithium has only one valence state (+1), and its isotope fractionation is not caused by primary productivity (Pogge von Strandmann et al., 2016), while it remains debatable whether plants can fractionate Li isotopes (Lemarchand et al., 2010; Clergue et al., 2015; Li et al., 2020; Pogge von Strandmann et al., 2021; Steinhoefel et al., 2021). This makes Li a useful

* Corresponding author.
*E-mail address:* qihuawen@vip.gyig.ac.cn (H.-W. Qi).

https://doi.org/10.1016/j.apgeochem.2022.105295
Received 21 October 2021; Received in revised form 11 March 2022; Accepted 4 April 2022
Available online 8 April 2022

chemical weathering tracer for silicate rocks (Misra and Froelich, 2012; Penniston-Dorland et al., 2017).

The Li elemental behavior in silicate chemical weathering is mainly controlled by primary mineral dissolution and secondary mineral precipitation. Previous experiments have shown that basalt primary mineral dissolution does not generally fractionate Li isotopes, whereas secondary mineral formation (e.g., clay minerals, Fe–Mn oxides) would preferentially enrich light Li isotopes (Vigier et al., 2008; Penniston-Dorland et al., 2017; Hindshaw et al., 2019; Pogge von Strandmann et al., 2020). This is because $Li^+$ in the fluid phase would form a stable tetrahedral complex, whose bond is stronger than the octahedral Li adsorbed onto the secondary mineral surface or entered the mineral lattice, and the heavier $^7Li$ preferentially enters high bond energy sites (Pistiner and Henderson, 2003; Wimpenny et al., 2010a; Liu et al., 2013; Zhang et al., 2021a). In addition, previous experimental studies also showed that different secondary minerals have different fractionation coefficients (α) for Li adsorption. For instance, kaolinite adsorption of Li at room temperature can produce a large fractionation ($\alpha = 0.992$, Pistiner and Henderson, 2003). Gibbsite selectively takes up $^6Li$ during the continuous adsorption/desorption process, causing major mineral-fluid isotope fractionation ($\alpha = 0.976$; Pistiner and Henderson, 2003; Huh et al., 2004). Recent studies showed that the Li isotope fractionation coefficient is influenced by both physical and chemical adsorption onto secondary minerals, which is in turn controlled by kinetic fractionation. The fractionation coefficient (0.992) is consistent with the degree of Li isotope fractionation between global basaltic river water and suspended loads (Hofmann et al., 2012; Pogge von Strandmann et al., 2017; Bohlin and Bickle, 2019; Hindshaw et al., 2019; Pogge von Strandmann et al., 2019; Li and Liu, 2020). In brief, secondary minerals take-up $^6Li$ preferentially, leading to lower $\delta^7Li$ in the solid weathering products than in river/seawater (Wang et al., 2015; Pogge-von Strandmann et al., 2017; Gou et al., 2019).

Previous Li isotope studies of basalt or diabase weathering profiles were mainly focused on those developed in Hawaii Island (Huh et al., 2004; Ryu et al., 2014; Li et al., 2020), South Carolina (Rudnick et al., 2004; Teng et al., 2010), Deccan Plateau (Kisakürek et al., 2004), Columbia River (Liu et al., 2013), Iceland (Pogge von Strandmann et al., 2012, 2021), or andesitic weathering profile in the Guadeloupe islands (Clergue et al., 2015). These studies have shown that Li isotopes are highly-fractionated during weathering, and that no isotope fractionation occurs during basalt dissolution (Pistiner and Henderson, 2003; Ryu et al., 2014). However, a weathering profile is an open system, and its chemical composition is influenced by factors such as the bedrock, climate, hydrology, biological action, topography, formation time, and external material input (e.g., aeolian dust and marine aerosol) (Pistiner and Henderson, 2003; Huh et al., 2004; Kisakürek et al., 2004; Rudnick et al., 2004; Liu et al., 2013; Clergue et al., 2015), which vary across different profiles (Ollier, 1988). Kinetic fractionation can also be brought by diffusion (Teng et al., 2010). The study of a series of basalt weathering profiles (with different rainfall) in Hawaii suggests that the relative atmospheric contribution in both dry and wet climate is minor (Ryu et al., 2014). However, a recent study on the same area suggests that biological uptake is important in the humid site, but atmospheric inputs were important in both humid and arid site (Li et al., 2020).

The tropical basalt weathering profile provides an ideal target for studying element activity and isotope fractionation at the extreme limit. We recently reported the mineralogical and geochemical (Jiang et al., 2018) and germanium isotope (Qi et al., 2019) variations across a well-developed basalt weathering profile (with soil, saprolite, semi-weathered basalt and fresh basalt horizons) at Wenchang on the tropical Hainan Island (South China). Here, we present high-precision Li isotope data from this profile, as well as sequential extraction results of representative samples, which enhance our understanding of Li isotope behavior under extreme chemical weathering conditions. In addition, considering that the atmospheric input (e.g., precipitation and aeolian deposition) has major influence on the basalt weathering profiles (Pistiner and Henderson, 2003; Huh et al., 2004; Kisakürek et al., 2004; Liu et al., 2013; Li et al., 2020), the radiogenic Sr isotopes of weathered products were also analyzed to constrain the external Li input.

## 2. Geological setting and sampling

The island of Hainan is the biggest tropical island in China, with a typical tropical ocean climate controlled by the East Asian monsoon, and a mean annual temperature of 25 °C and mean precipitation of 1500 mm (800–2500 mm, >80% occurs from May to October) (Ma et al., 2007). The southward aeolian transport from the Loess Plateau in North China and marine aerosol from the South China Sea dominant the atmospheric input of this area (Ma et al., 2007; Li et al., 2016). Cenozoic basalts are widely distributed in northern Hainan (Liu et al., 2015), and are commonly covered by laterite derived from basalt weathering (Fig. 1a).

The studied profile (thickness: up to 19.73 m) is located in a quarry and developed on the Miocene-Pliocene tholeiitic basalt in southwestern Wenchang (19°34′47.0"N, 110°38′42.6"E; Fig. 1a–b). Detailed descriptions of the profile (including horizon, soil color and structure, influence of biological activity, mineral and bulk-sample composition) are given in Jiang et al. (2018). Two discontinuities in color, clay mineralogy and major and trace element composition are present at the soil-saprolite (2.4 m depth) and rock-regolith (15.28 m depth) interfaces, and the profile comprises mainly three horizons, i.e., soil (A-horizon), saprolite (B-horizon), semi-weathered basalt (C-horizon) and fresh basalt (Fig. 1c).

The top 2.4 m of the profile comprises reddish homogenous soil. The soil-saprolite interface is characterized by the highest contents of $Al_2O_3$, $Fe_2O_3$, $TiO_2$, LOI and Cr, and the lowest content of $SiO_2$. This interface is also marked by the dominance of gibbsite and Fe-oxides/-hydroxides and the color change from dark brick-red to light brick-red. The color of the saprolite changes from deep-red at 2.4–13.2 m to yellowish at 13.2–15.28 m. Secondary carbonate precipitation occurred at 3.9 m and 7.1 m depth, and secondary Mn-oxides/-hydroxides precipitated at 6.1 m depth with enrichments in Co, Ba, Cu, Ni, Li and Sc. The rock-regolith interface is marked by the yellowish semi-weathered basalt (C-horizon) above the fresh basalt, and contains secondary phosphates and distinct enrichments in Be, Cu, Zn, Ni, Sc and V (Jiang et al., 2018). The fresh basalts comprise predominantly plagioclase and pyroxene. Toward the surface, with increasing weathering intensity, the primary minerals were broken down and secondary minerals (kaolinite, gibbsite, smectite and Fe–Mn oxides/-hydroxides) dominate. The chemical index of alteration (CIA) of the weathering products is very high (~100%) (Table 1; Fig. 2h), suggesting intensive weathering (Jiang et al., 2018).

The sampling interval for the 12 soil samples (WC-1 to WC-12) and 19 saprolite samples (WC-13 to WC-31) is 15–20 cm apart, while saprolite samples WC-32 to WC-52 were collected continually down depth. Each sample is about 20 cm (length) × 20 cm (width) × 15–20 cm (height). One semi-weathered basalt (WC-53) and five fresh basalts (WC-54 to WC-58) were sampled in a 0.6–1.3 m spacing (Fig. 1c). The soil and saprolite samples collected were dried at room temperature, and milled to 200 mesh (<75 μm) with a tungsten-carbide mill after removing organic materials such as plant roots and stems.

## 3. Analytical methods

### 3.1. Lithium elemental and isotopic analyses

Lithium isotope analysis was conducted at the CAS Laboratory of Crust-Mantle Materials and Environments, University of Science and Technology of China (USTC, Hefei), following the procedures described by previous studies (Gao and Casey, 2012; Sun et al., 2016; Tong et al., 2021). Briefly, ~50 mg of powdered material was weighed into individual 7 ml PFA Teflon beakers (Savillex) and digested with a mixture of optimal-grade concentration HF + $HNO_3$+$HClO_4$ at 150 °C to remove the silicon and organic matter. Concentrated $HNO_3$ and HCl (1 and 3 ml,

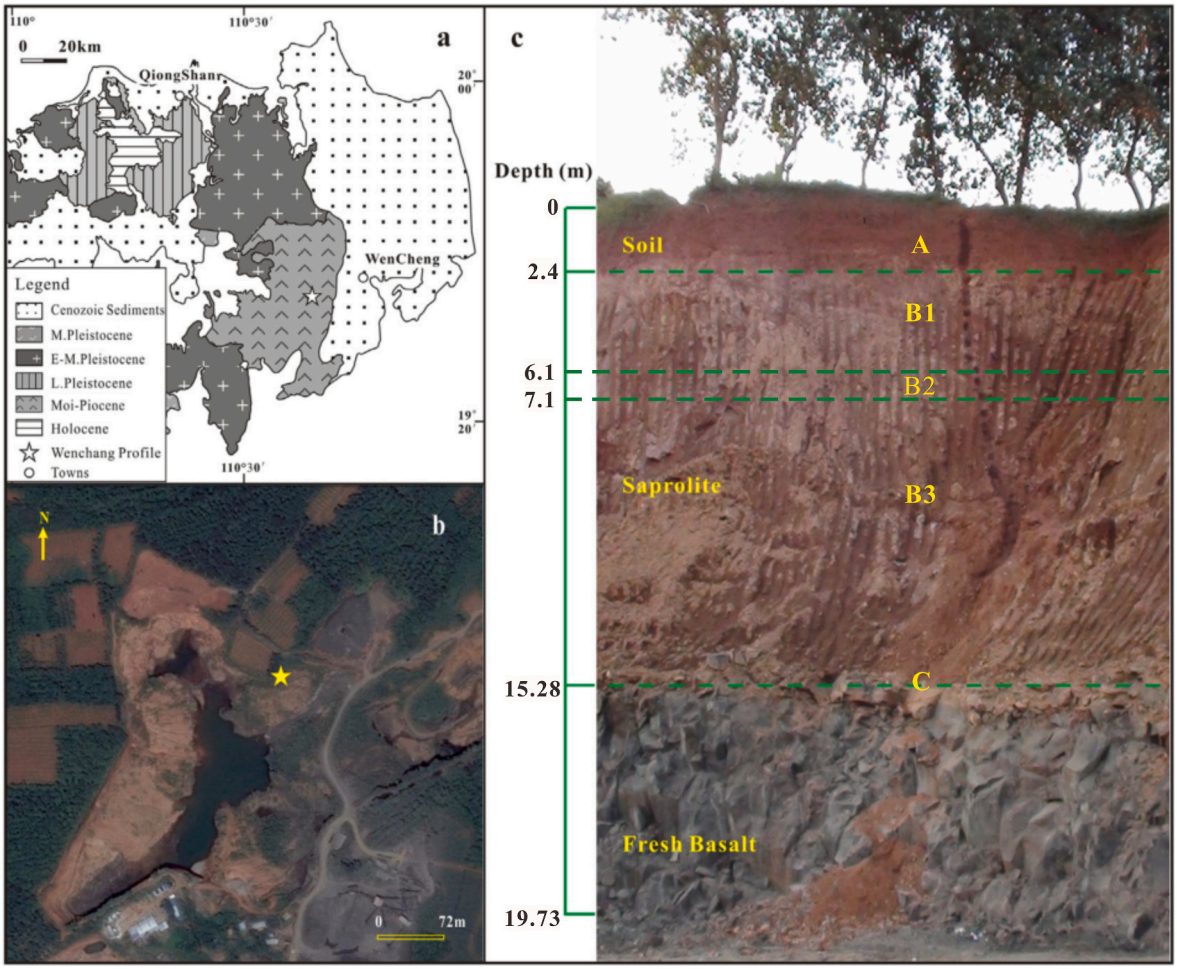


**Fig. 1.** (a) Simplified geologic map and sampling location in Wenchang, northern Hainan Island (modified after Liu et al., 2015); (b) Google Earth satellite image of sampling site; (c) Outcrop photo of the Wenchang basalt weathering profile (after Jiang et al., 2018). A, B1, B2, B3, C and fresh basalt represent the regolith division adopted in this study.

respectively) were then added, and the capped beakers were heated at 150 °C for ~12 h; this was repeated until the solution was clarified. Chemical separation of Li was achieved with an organic solvent-free two-step liquid chromatography procedure in a Class 1000 clean lab in the USTC. The columns were filled with Bio-Rad AG 50W-X8 resin (200–400 mesh) as the first step column and Bio-Rad AG 50W-X12 resins (200–400 mesh) as the second one, and 0.2 mol/l ultra-pure HCl was chosen as the eluent (Gao and Casey, 2012; Sun et al., 2016; Tong et al., 2021). Subsequently, the Li content of these samples was measured by ICP-MS. All separations yielded complete Li recovery (>99.8%) and low Na/Li ratio (<0.5). The purified Li solutions were adjusted to ~100 ppb by adding 2% $HNO_3$ before measuring with a Thermo Scientific Neptune Plus multi-collector (MC)-ICP-MS. Samples were introduced through a low-flow PFA nebulizer (~50 μL/min) coupled with a quartz spray chamber, and the Faraday cups L4 and H4 were used to collect the $^{6}Li$ and $^{7}Li$ signal, respectively. The sample-standard bracketing method was used with 100 ppb L-SVEC standard, and the total procedural blank was <5 pg Li. The results were reported as $\delta^{7}Li = (((^{7}Li/^{6}Li)_{sample}/(^{7}Li/^{6}Li)_{standard}-1)*1000‰$, using LSVEC as the standard. The long-term external precision is better than ± 0.3‰ (Gao and Casey, 2012; Sun et al., 2016; Tong et al., 2021). Repeated analysis of international rock standards yielded $\delta^{7}Li$ = +2.4 ± 0.3‰ (2SD; n = 3) for BCR-2, -0.5 ± 0.3‰ for GSP-2, +4.0 ± 0.3‰ (2SD; n = 2) for BHVO-2, and +1.8 ± 0.3‰ for GSR-1, which agree with the recommended values within error (BCR-2: 3.13 ± 1.01‰; GSP-2: 0.79 ± 0.24‰; BHVO-2: 4.54 ± 0.27‰; GSR-1: 1.53 ± 0.26‰) (GeoREM: http://georem.mpch-mainz.gwdg.de; Zhu et al., 2019).

### 3.2. Strontium isotope analyses

The strontium isotope ratio ($^{87}Sr/^{86}Sr$) analysis was performed at the State Key Laboratory of Ore Deposit Geochemistry, Institute of Geochemistry, Chinese Academy of Sciences (IGCAS). About 120–130 mg sample powder was weighted and dissolved by 15 ml HF + $HNO_3$+$HClO_4$ in Teflon bombs for 7 day at 200 °C, before being separated by a cation exchange column (Bio-Rad AG 50W*12). The isotopic ratios were determined with a Thermo Fisher Scientific Neptune Plus MC-ICP-MS. To ensure the measurement accuracy and reproducibility, the NIST SRM 987 carbonate strontium isotope standard was measured with the samples, which yielded a mean $^{87}Sr/^{86}Sr$ = 0.710261 ± 15 (2SD, n = 4). The geochemical reference material BCR-2 (basalt) yielded a mean $^{87}Sr/^{86}Sr$ = 0.705029 ± 30 (2SD, n = 2), consistent with the recommended value (0.705023 ± 13, Yang et al., 2010).

### 3.3. Sequential extraction analysis

To understand the different association of Li along depth of the profile, we selected samples from near the interfaces and high-Mn samples for the sequential extraction analysis (Fig. 2a and c). The analysis was conducted at the State Key Laboratory of Environmental Geochemistry of IGCAS. A modified BCR method (following Ure et al., 1993; Cuong and Obbard, 2006; Pueyo et al., 2008) was used. In brief,

**Table 1**
Selected major and trace element concentrations, $\delta^7Li$,$^{87}Sr/^{86}Sr$, CIA and Ce/Ce* for weathering products from the Wenchang basalt weathering profile.

| Sample ID | Depth (m) | Sample type | Horizon | $Fe_2O_3$ (%) | MnO (%) | Li (μg/g) | Nb (μg/g) | CIA[b] (%) | $\delta^7Li$ (‰) | 2SD | $^{87}Sr/^{86}Sr$ | Ce/Ce*[c] | 2SD |
|---|---|---|---|---|---|---|---|---|---|---|---|---|---|
| WC-1 | 0.1 | Soil | A | 22.2 | 0.14 | 2.6 | 58.0 | 99.4 | 1.5 | 0.3 | 0.70568 | 1.08 | 0.14 |
| WC-2 | 0.3 | Soil | A | 22.9 | 0.18 | 3.6 | 57.3 | 99.8 | 2.6 | 0.3 | | 1.15 | 0.15 |
| WC-3 | 0.5 | Soil | A | 22.5 | 0.19 | 2.6 | 52.2 | 99.9 | 2.0 | 0.3 | 0.70587 | 1.23 | 0.16 |
| WC-4 | 0.7 | Soil | A | 22.5 | 0.18 | 3.7 | 53.4 | 99.9 | 1.8 | 0.3 | | 1.27 | 0.16 |
| WC-5 | 0.9 | Soil | A | 22.6 | 0.20 | 3.2 | 51.6 | 99.9 | 2.1 | 0.3 | 0.70589 | 1.30 | 0.17 |
| WC-6 | 1.1 | Soil | A | 22.4 | 0.21 | 3.8 | 48.4 | 99.9 | 0.7 | 0.3 | | 1.35 | 0.18 |
| WC-7 | 1.3 | Soil | A | 24.2 | 0.19 | 2.7 | 43.4 | 99.8 | 0.1 | 0.3 | 0.70619 | 1.40 | 0.18 |
| WC-8 | 1.5 | Soil | A | 21.6 | 0.16 | 3.6 | 42.3 | 99.9 | 0.9 | 0.3 | | 1.51 | 0.20 |
| WC-9 | 1.7 | Soil | A | 21.7 | 0.14 | 3.5 | 42.3 | 99.9 | 0.9 | 0.3 | 0.70618 | 1.81 | 0.23 |
| WC-10 | 1.9 | Soil | A | 21.6 | 0.16 | 2.6 | 40.8 | 99.9 | −1.3 | 0.3 | | 1.73 | 0.22 |
| WC-11 | 2.1 | Soil | A | 22.7 | 0.19 | 3.0 | 41.4 | 99.8 | −6.2 | 0.3 | | 1.88 | 0.24 |
| WC-12 | 2.4 | Soil | A | 28.5 | 0.13 | 2.2 | 51.8 | 99.9 | −1.6 | 0.3 | 0.70632 | 1.66 | 0.22 |
| WC-13 | 2.8 | Saprolite | B1 | 20.9 | 0.38 | 4.6 | 36.1 | 99.9 | −9.1 | 0.3 | 0.70762 | 3.50 | 0.45 |
| WC-14 | 3.1 | Saprolite | B1 | 22.3 | 0.21 | 3.5 | 40.7 | 99.9 | 1.3 | 0.3 | 0.70673 | 3.14 | 0.41 |
| WC-15 | 3.5 | Saprolite | B1 | 19.6 | 0.43 | 5.2 | 38.5 | 99.9 | −6.9 | 0.3 | | 1.86 | 0.24 |
| WC-16 | 3.9 | Saprolite | B1 | 22.2 | 0.31 | 8.7 | 52.1 | 99.8 | −8.0 | 0.3 | 0.70585 | 0.57 | 0.07 |
| WC-17 | 4.4 | Saprolite | B1 | 22.3 | 0.19 | 2.8 | 49.6 | 99.9 | 5.5 | 0.3 | | 0.77 | 0.10 |
| WC-18 | 4.9 | Saprolite | B1 | 17.2 | 0.13 | 4.4 | 36.8 | 100 | 3.3 | 0.3 | 0.70514 | 1.75 | 0.23 |
| WC-19 | 5.3 | Saprolite | B1 | 20.2 | 0.23 | 4.8 | 38.9 | 100 | −3.5 | 0.3 | | 3.18 | 0.41 |
| WC-20 | 5.7 | Saprolite | B1 | 21.1 | 0.23 | 4.3 | 39.2 | 99.9 | 4.3 | 0.3 | 0.70538 | 5.24 | 0.68 |
| WC-21 | 6.1 | Saprolite | B2 | 20.1 | 1.82 | 58.1 | 36.9 | 99.9 | −14.3 | 0.3 | 0.70520 | 3.75 | 0.49 |
| WC-22 | 6.7 | Saprolite | B2 | 19.1 | 0.47 | 19.6 | 37.3 | 99.9 | −14.1 | 0.3 | 0.70496 | 1.72 | 0.22 |
| WC-23 | 7.1 | Saprolite | B2 | 18.6 | 0.32 | 11.3 | 43.9 | 99.9 | −12.0 | 0.3 | 0.70495 | 0.57 | 0.07 |
| WC-24 | 7.3 | Saprolite | B3 | 21.3 | 0.29 | 4.9 | 47.1 | 99.9 | −5.5 | 0.3 | | 1.27 | 0.16 |
| WC-25 | 7.5 | Saprolite | B3 | 21.9 | 0.19 | 4.0 | 47.1 | 99.9 | 6.1 | 0.3 | 0.70505 | 1.02 | 0.13 |
| WC-26 | 8 | Saprolite | B3 | 21.4 | 0.28 | 5.2 | 45.5 | 99.9 | −2.6 | 0.3 | | 1.58 | 0.21 |
| WC-27 | 8.4 | Saprolite | B3 | 22.6 | 0.21 | 4.7 | 46.0 | 99.9 | 7.0 | 0.4 | 0.70510 | 0.94 | 0.12 |
| WC-28 | 8.6 | Saprolite | B3 | 24.2 | 0.29 | 3.4 | 47.5 | 99.9 | 5.7 | 0.3 | | 2.15 | 0.28 |
| WC-29 | 8.8 | Saprolite | B3 | 21.5 | 0.19 | 3.0 | 47.7 | 99.8 | 6.3 | 0.3 | 0.70512 | 1.07 | 0.14 |
| WC-30 | 9.1 | Saprolite | B3 | 21.1 | 0.23 | 2.8 | 39.8 | 99.9 | 7.0 | 0.3 | | 1.15 | 0.15 |
| WC-31 | 9.28 | Saprolite | B3 | 21.1 | 0.20 | 2.8 | 43.4 | 99.9 | 6.9 | 0.3 | 0.70507 | 0.91 | 0.12 |
| WC-32 | 9.56 | Saprolite | B3 | 21.2 | 0.24 | 3.0 | 45.8 | 99.7 | 7.6 | 0.3 | | 0.78 | 0.10 |
| WC-33 | 9.84 | Saprolite | B3 | 20.6 | 0.28 | 3.2 | 42.7 | 99.9 | 8.9 | 0.4 | | 0.96 | 0.12 |
| WC-34 | 10.12 | Saprolite | B3 | 21.9 | 0.38 | 3.5 | 42.3 | 99.8 | 6.8 | 0.3 | 0.70518 | 1.32 | 0.17 |
| WC-35 | 10.4 | Saprolite | B3 | 23.0 | 0.40 | 2.9 | 42.8 | 99.9 | 5.7 | 0.3 | | 1.17 | 0.15 |
| WC-36 | 10.68 | Saprolite | B3 | 21.7 | 0.26 | 2.9 | 40.9 | 99.9 | 6.8 | 0.3 | 0.70638 | 5.18 | 0.67 |
| WC-37 | 10.96 | Saprolite | B3 | 21.6 | 0.27 | 2.6 | 39.1 | 99.9 | 5.3 | 0.3 | | 2.45 | 0.32 |
| WC-38 | 11.24 | Saprolite | B3 | 20.7 | 0.28 | 2.9 | 43.6 | 99.9 | 4.5 | 0.3 | 0.70608 | 1.01 | 0.13 |
| WC-39 | 11.52 | Saprolite | B3 | 22.0 | 0.33 | 3.0 | 47.4 | 99.9 | 2.1 | 0.3 | | 1.15 | 0.15 |
| WC-40 | 11.8 | Saprolite | B3 | 21.5 | 0.27 | 3.5 | 40.3 | 99.9 | 3.2 | 0.3 | 0.70610 | 1.03 | 0.13 |
| WC-41 | 12.08 | Saprolite | B3 | 21.4 | 0.37 | 4.1 | 42.6 | 99.9 | 1.1 | 0.3 | | 1.25 | 0.16 |
| WC-42 | 12.36 | Saprolite | B3 | 21.2 | 0.28 | 2.9 | 38.5 | 99.7 | 3.1 | 0.3 | 0.70606 | 1.13 | 0.15 |
| WC-43 | 12.64 | Saprolite | B3 | 20.2 | 0.26 | 4.0 | 35.6 | 99,.7 | −0.9 | 0.3 | | 1.03 | 0.13 |
| WC-44 | 12.92 | Saprolite | B3 | 22.1 | 0.57 | 3.8 | 44.5 | 99.8 | −0.7 | 0.3 | 0.70544 | 1.43 | 0.19 |
| WC-45 | 13.2 | Saprolite | B3 | 21.5 | 0.26 | 3.7 | 43.4 | 99.9 | −2.6 | 0.3 | | 1.57 | 0.20 |
| WC-46 | 13.48 | Saprolite | B3 | 19.7 | 0.28 | 3.0 | 39.7 | 99.9 | −5.0 | 0.3 | 0.70574 | 1.05 | 0.14 |
| WC-47 | 13.76 | Saprolite | B3 | 21.3 | 0.30 | 3.7 | 40.7 | 99.8 | −4.8 | 0.3 | | 0.64 | 0.08 |
| WC-48 | 14.04 | Saprolite | B3 | 19.7 | 0.33 | 3.7 | 35.9 | 99.7 | −4.0 | 0.3 | 0.70598 | 1.05 | 0.14 |
| WC-49 | 14.32 | Saprolite | B3 | 21.1 | 0.27 | 4.4 | 39.4 | 99.8 | −9.6 | 0.3 | | 1.36 | 0.18 |
| WC-50 | 14.6 | Saprolite | B3 | 20.9 | 0.44 | 4.1 | 38.0 | 99.7 | −5.2 | 0.3 | 0.70579 | 0.32 | 0.04 |
| WC-51 | 14.88 | Saprolite | B3 | 20.5 | 0.14 | 4.2 | 45.2 | 99.7 | −3.2 | 0.3 | 0.70571 | 0.25 | 0.03 |
| WC-52 | 15.16 | Saprolite | B3 | 18.1 | 0.28 | 4.4 | 35.7 | 99.7 | −1.5 | 0.3 | 0.70560 | 0.59 | 0.08 |
| WC-53 | 15.28 | SWB[a] | C | 14.8 | 0.12 | 33.7 | 31.4 | 69.1 | −2.7 | 0.3 | 0.70460 | 0.22 | 0.03 |
| WC-54 | 15.83 | Basalt | R | 11.0 | 0.12 | 4.7 | 24.7 | 40.3 | 2.3 | 0.3 | 0.70442 | 1 | 0.13 |
| WC-55 | 16.43 | Basalt | R | 11.3 | 0.17 | 5.2 | 23.9 | 40.1 | 3.8 | 0.3 | | 0.99 | 0.13 |
| WC-56 | 17.43 | Basalt | R | 11.7 | 0.13 | 5.3 | 22.9 | 40.9 | 0.7 | 0.3 | | 1.02 | 0.13 |
| WC-57 | 18.73 | Basalt | R | 11.5 | 0.15 | 4.7 | 24.4 | 40.4 | 2.8 | 0.3 | | 0.99 | 0.13 |
| WC-58 | 19.73 | Basalt | R | 11.5 | 0.15 | 4.0 | 22.4 | 40.5 | 5.3 | 0.3 | 0.70456 | 1 | 0.13 |

[a] SWB = Semi-weathered.
[b] CIA was calculated by Equation (2) in section 3.4.
[C] Ce/Ce* was calculated by Equation (3) in section 3.4.

the exchangeable phase was leached with 0.11 mol/l HOAc for 24 h; reducible Fe/Mn (hydr)-oxides was leached with 0.5 mol/l $NH_2OH{\cdot}HCl$ at pH 1.5 for 24 h; organic matter phase was leached with 30%(v/v) $H_2O_2$ in 1.0 mol/l $NH_4OAc$ at pH 2–3 and 85 °C for 2–3 h, and the residual silicate phase was dissolved by concentrated $HNO_3$ and HF at 160 °C for 48 h. After drying and sieving, about 0.5 g air-dried soil sample was weighted in a 50-ml centrifuge tube, and the reagents were added sequentially. For the first three steps, the tubes (with the reagents) were shaken for ~24 h at room temperature (25 °C), and then the supernatant was collected after the centrifugation. For step 4, the residue after centrifugation was cleaned three times with ultra-pure water (18.2 MΩ cm), and then dried in a freeze dryer (EYELA FDU-2110, Japan) for 24 h. After that, the samples were sieved, and the fine powder (200 mesh) was digested, following the same procedure as the bulk sample (Cuong and Obbard, 2006). About 50 mg sample powder was acid-digested in a Teflon beaker with a mixture of 3 ml concentrated $HNO_3$ and 1 ml HF at 160 °C for 48 h. Subsequently, the resulting fluorides were removed after cooling and drying (and then re-drying after adding 1 ml $HNO_3$) over a hotplate, and ultra-pure water (4 ml) and $HNO_3$ (1 ml) were added to dissolve any residue. The digest

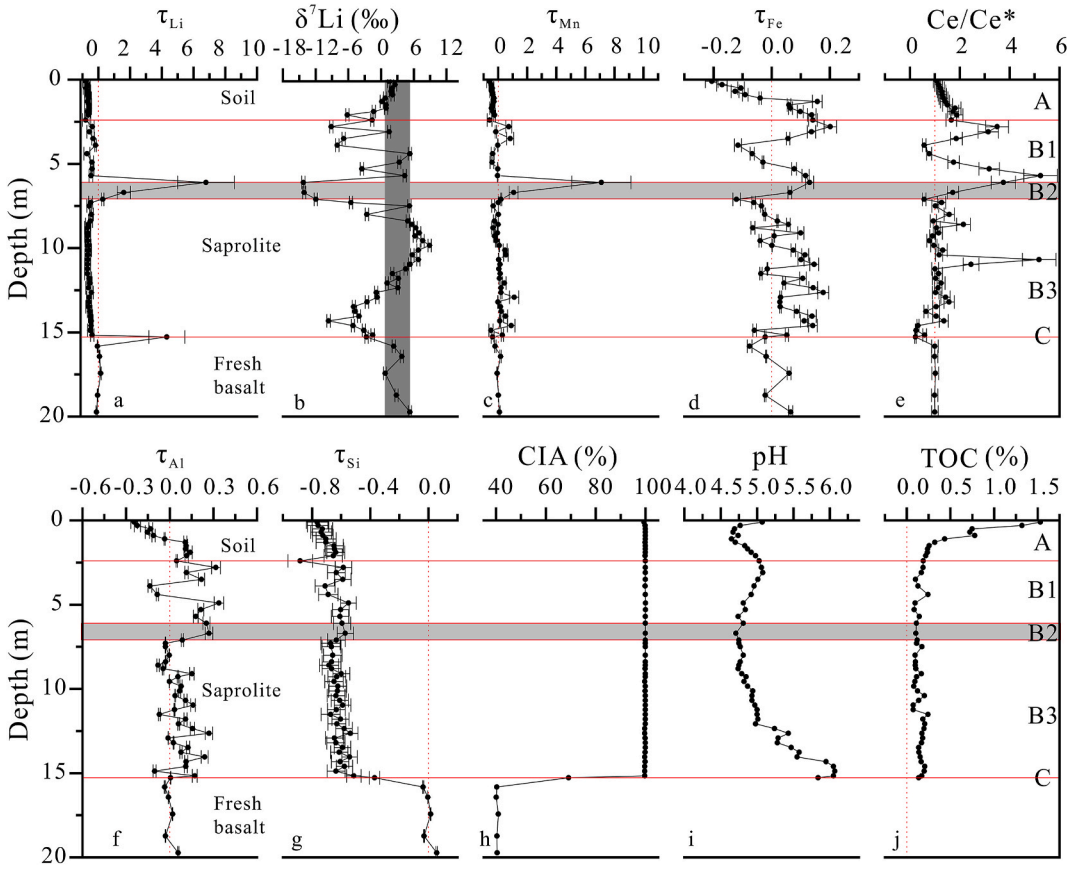


**Fig. 2.** Vertical variations of (a) $\tau_{Li}$, (b) $\delta^7Li$, (c) $\tau_{Mn}$, (d) $\tau_{Fe}$, (e) Ce/Ce*, (f) $\tau_{Al}$, (g) $\tau_{Si}$, (h) CIA, (i) TOC and (j) pH values across the Wenchang basalt weathering profile. The mass transfer coefficient ($\tau$) is calculated with Equation (1). Red dashed line denotes $\tau = 0$, the horizontal red line denotes the interface of each horizon, horizontal light grey bar denotes Li-enriched horizon (B2-horizon), whilst the vertical dark grey bar denotes the fresh basalt $\delta^7Li$ range. Ce/Ce* (Ce anomaly) and CIA values are listed in Table 1. Error bars are 2SD for $\tau_{Li}$, $\delta^7Li$, $\tau_{Mn}$, $\tau_{Fe}$, Ce/Ce*,$\tau_{Al}$, and $\tau_{Si}$. (For interpretation of the references to color in this figure legend, the reader is referred to the Web version of this article.)

solution was transferred into a centrifugal tube, and then the trace element concentrations were measured with ICP-MS at the State Key Laboratory of Environmental Geochemistry (IGCAS) after diluting. All the bottles and glassware used were thoroughly cleaned with dilute nitric acid (30%, v/v) for over 24 h, and then rinsed with ultra-pure water (18.2 MΩ cm) for more than three times. All the reagents are of ultrapure grade to ensure low procedural blank.

### 3.4. Element mobilization and re-distribution

The factor $\tau_{j,w}$ can be used to estimate the gain ($\tau_{j,w} > 0$) or loss ($\tau_{j,w} < 0$) relative to the fresh basalt of element (j) (Brimhall and Dietrich, 1987; Chadwick et al., 1990), and can be expressed as:

$$\tau_{j,w} = \frac{C_{j,w}}{C_{j,p}} \times \frac{C_{i,p}}{C_{i,w}} - 1 \quad (1)$$

where $C_{j,w}$ and $C_{j,p}$ = element $j$ content in the weathered soil and fresh basalt, $C_{i,w}$ and $C_{i,p}$ = immobile element $i$ content in the weathered soil and fresh basalt, respectively. In this study, niobium was chosen as the immobile element $i$, following Kurtz et al. (2000) and Jiang et al. (2018). The average basaltic elemental concentrations and Nb concentration were adopted for the $C_{j,p}$ and $C_{i,p}$ of the fresh basalts, respectively.

The chemical index of alteration (CIA) was used to evaluated weathering intensity (Nesbitt and Young, 1982). It is calculated using molecular proportions and the following equation:

$$CIA = Al_2O_3/(Al_2O_3 + CaO^* + Na_2O + K_2O) \times 100\% \quad (2)$$

where CaO* is the amount of CaO incorporated in the silicate fraction of the rock (Nesbitt and Young, 1982). Correction for Ca in apatite is done on the basis of the $P_2O_5$ content, and Ca from carbonates was not corrected because little carbonate is present in the weathered products (McLennan, 1993; Rudnick et al., 2004; Qi et al., 2019).

The change of redox condition can be estimated by the $\tau$ values of redox-sensitive elements (e.g., Mn, Fe, Co) and Ce/Ce* (as a proxy of oxidation conditions, Wang et al., 2018):

$$Ce/Ce^* = Ce_N/(La_N \times Pr_N)^{0.5} \quad (3)$$

where N represents normalized to the average of fresh basalts.

## 4. Results

The extremely high CIA values (~100%, Table 1), high $Al_2O_3$ and $Fe_2O_3$ concentrations (up to 32.3% and 28.5%, respectively, Jiang et al., 2018) and kaolinite, Fe-oxides/-hydroxides and gibbsite (or boehmite) dominate mineral assemblage (Jiang et al., 2018) of Wenchang weathering products, indicate a highly weathered setting. Under extreme tropical weathering condition, mobile elements (e.g., Na, K, Ca, Mg, Rb, Sr) are largely leached out of the profile, whose $\tau$ values are mostly negative (some approaching-1). However, lithium, some redox-sensitive elements and immobile elements (e.g., Fe, Mn, Ce, Co), are enriched in the middle section of the profile (6.1 m depth), as well as at the soil-saprolite (2.4 m depth) and rock-regolith (15.28 m depth) interfaces (Table 1; Fig. 2). Accordingly, we divide the profile into five horizons: A (0–2.4 m); B1 (2.4–6.1 m); B2 (6.1–7.1 m); B3 (7.1–15.28 m); C (15.28

m) and fresh basalt (>15.28 m).

### 4.1. Lithium concentration

Bulk Li contents of soil and saprolite samples vary with depth, ranging from 2.2 to 58.1 ppm (Table 1), most of which are lower than the semi-weathered basalt (33.7 ppm) and fresh basalt (4.0–5.2 ppm, avg 4.6 ppm, n = 5). Lithium concentration of the fresh basalt is higher than that (1.39 ± 0.10 ppm) of fresh MORB (Marschall et al., 2017). Most calculated $\tau_{Li}$ values for these samples are negative, indicating significant Li depletion relative to the fresh basalt (Table 1; Fig. 2a). However, two distinct enrichment peaks are present at 6.1 m depth ($\tau_{Li}$ = 7.12), where the Mn–Co contents are also high ($\tau_{Mn}$ = 7.10, $\tau_{Co}$ = 19.14), and at 15.28 m depth in the semi-weathered basalt (WC-53) ($\tau_{Li}$ = 4.54) (Table 1; Fig. 2c and h).

### 4.2. Lithium isotope compositions

The $\delta^7$Li values of soil and saprolite samples range from −14.3 to 8.9‰, exhibiting complex fluctuations with depth (Fig. 2b). The values generally decrease from the surface (2.6‰) to the soil-saprolite interface (−6.2‰) in A-horizon, fluctuate within the B1-horizon, and then reach a minimum (−14.25‰) in B2-horizon (where Mn–Co enrichment occurs). Below that, $\delta^7$Li increases with depth and reaches a maximum (8.9‰) at 9.84 m depth, and then decrease again to −9.6‰ near the rock-regolith interface. The semi-weathered basalt has $\delta^7$Li = −2.7‰, and five fresh basalt samples have $\delta^7$Li = 0.7–5.3‰ (avg 3.0‰), within the range (for basalt) reported by Liu et al. (2013).

### 4.3. Strontium isotope compositions

The $^{87}Sr/^{86}Sr$ values of the soil and saprolite samples range from 0.70496 to 0.70761, and those in the upper (A- and B1-horizons) and lower (lower B3-horizon) parts of the profile are higher than those in the middle part (B2-horizon and upper B3-horizon). These $^{87}Sr/^{86}Sr$ values are higher than those of the semi-weathered basalt (0.70460) and fresh basalt (0.70442–0.70456), but lower than that of sea-salt aerosol (Table 1; Fig. 3b).

### 4.4. Sequential extraction results

The sequential extraction results of 10 representative samples are listed in Table S2. Most soil Li was found in the residual fraction, 6.5–88.9% of total Li, followed by Fe–Mn oxides (1.6–71.9%) and organically bound (3.9–27.0%). Exchangeable phase only contains 0.2–2.0% of total Li. Among the samples, lithium in A-horizon (WC-1 and WC-12), B3-horizon (WC-38 and WC-52) and C-horizon (WC-53) mainly exists in residual phase, while most Li in the B1-horizon (WC-13, WC-15) and B2-horizon (WC-21 and WC-22) of the profile exists in Fe–Mn oxide phases (Fig. 4a). The samples with high Fe–Mn oxide content (> 50%) or higher bulk $\tau_{Mn}$ values tend to have lower bulk $\delta^7$Li values (Fig. 4b and c).

## 5. Discussion

As a mobile element, lithium is mostly leached during weathering in the studied profile. However, samples in B2- and C-horizons are abnormally Li-rich. The Li isotope compositions vary in different horizons, and there is an overall positive 1/Li vs. $\delta^7$Li correlation in the soil and saprolite samples (Fig. 5), which indicate the occurrence of other processes (e.g., adsorption and desorption) during the weathering (Rudnick et al., 2004), since the $\delta^7$Li values of weathered products would decrease with continuously leaching (positive Li vs. $\delta^7$Li correlation). Here, we discuss the controlling factors on the Li elemental and isotopic distributions during extreme weathering of basalts.

### 5.1. Atmospheric input

Previous studies have shown that atmospheric input with high Li content and different Li isotope compositions have major influence on the basalt weathering profiles in Hawaii (Huh et al., 2004; Li et al., 2020; Pistiner and Henderson, 2003), Columbia river (Liu et al., 2013), and Bidar (Kisakürek et al., 2004). As for the Wenchang profile, dry deposit (e.g., Asian dust (Chinese loess)) and/or wet deposit (e.g., marine aerosol) may have contributed chemically to the weathering products.

Possible contribution from the Chinese loess can be evaluated by comparing the immobile element contents between the loess and the basalt weathering products at Wenchang (Wang et al., 2018). In the

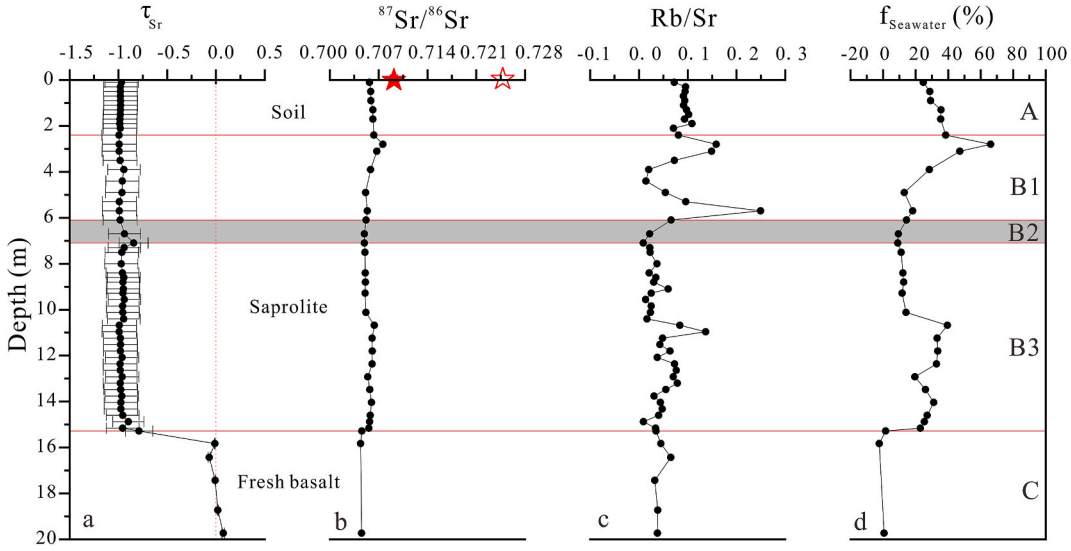


**Fig. 3.** Vertical variations of the (a) $\tau_{Sr}$, (b) $^{87}Sr/^{86}Sr$, (c) Rb/Sr, and (d) $f_{Seawater}$ values in the Wenchang basalt weathering profile. Red vertical dashed-line denotes $\tau$ = 0, the horizontal red line denotes the interface of each horizon, horizontal light grey bar denotes Li-enriched (B2) horizon, whilst the solid star represents the sea-salt aerosol $^{87}Sr/^{86}Sr$ value (0.710; Biscaye et al., 1997), and the hollow star represents the dust $^{87}Sr/^{86}Sr$ value (0.725; Sun 2005), the mass fraction of the marine aerosol-derived Sr ($f^{Sr}_{seawater}$) was calculated by equation (4). Error bars are 2SD for $\tau_{Sr}$. (For interpretation of the references to color in this figure legend, the reader is referred to the Web version of this article.)

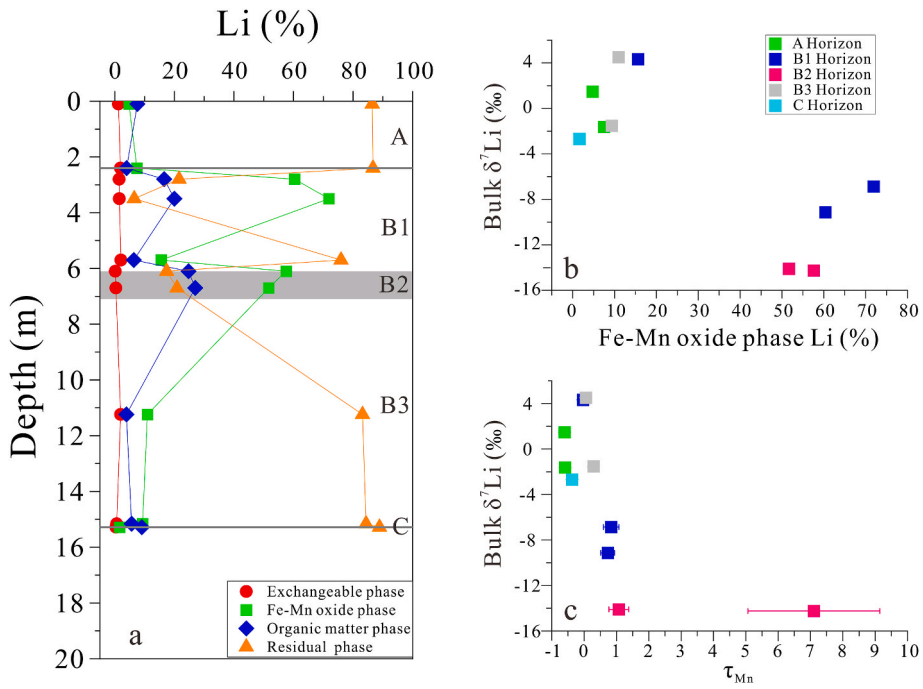


**Fig. 4.** (a) Depth variations of the relative proportions of Li in soil extractions of the Wenchang basalt weathering profile. (b) Li content in the Fe–Mn oxide phase (%) vs. bulk $\delta^7$Li. (c) $\tau_{Mn}$ vs. bulk $\delta^7$Li. Error bars are 2SD for $\tau_{Mn}$.

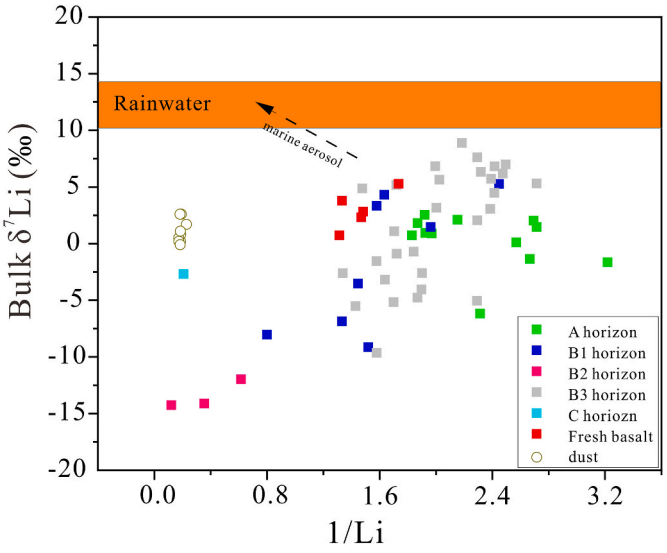


**Fig. 5.** $\delta^7$Li vs. molar 1/Li for the weathering products from the Wenchang basalt weathering profile. Dust values are from the loess of North China (Sauzéat et al., 2015), and rain values are from South China (Zhang et al., 2021a).

ternary La–Th-Sc diagram, it is shown that the immobile element compositions of the Wenchang weathering products are distinct from those of the loess (Fig. 6a). The nearly constant Th/Nb and Nb/Ta ratios for most soil and saprolite samples also support such suggestion (Jiang et al., 2018). The average Li contents and $\delta^7$Li of the loess are similar to the UCC (upper continental crust) value, with Li = 30.5 ppm; $\delta^7$Li = 0.6 ± 0.6 (2σ) (Teng et al., 2004; Tasi et al., 2014; Sauzéat et al., 2015; He et al., 2021). The $\delta^7$Li values of the Wenchang near-surface soil samples are higher than that of the average Chinese loess. These, together with the different $^{87}Sr/^{86}Sr$ values of the weathering products from the dust end-member (0.7246) (Sun, 2005), we demonstrate that aeolian dust has little influence on the Li isotopes of the Wenchang samples. This conclusion is consistent with that drawn from the Zhanjiang basalt weathering profile (China), whose Asian aeolian dust contribution was estimated to be < 3.5% (Tong et al., 2021).

Generally, the rainwater Li isotopes (+3.2 to + 95.6‰, avg. + 18‰) are heavier than those of the regolith, and the rainwater Li content is of 0.004–0.142 nmol $^{-1}$ (Pistiner and Henderson, 2003; Millot et al., 2010a; Clergue et al., 2015; Tong et al., 2021; Zhang et al., 2021a). With rainwater input, the $\delta^7$Li of A-horizon would show an upward increasing trend (Huh et al., 2004; Clergue et al., 2015; Li et al., 2020). Considering that the study area is close to the South China Sea (<20 km), marine aerosol has likely major Li input to the profile. Here, the calculation method for marine aerosol Li input by Pistiner and Henderson (2003) and Zhang et al. (2021a) was adopted, using the basalt age of 4 Ma, mean annual precipitation of 150 cm (Jiang et al., 2018), and the rainwater Li content of 0.82 μg/L (Zhang et al., 2021a). The calculation yielded a Li input of 492 mg cm$^{-2}$ into the profile, and an average Li input of up to 214 ppm for the whole profile.

However, the Li content (<5 ppm) in most weathering products at Wenchang is much lower than the above calculated value, and shows an upward decreasing trend. The $\delta^7$Li value of the regolith increases toward the surface in A-horizon, much lower than that of seawater (31.1 ± 0.2‰) (Jeffcoate et al., 2004) and unfiltered rainwater from South China (+6.1 and + 9.1‰) (Zhang et al., 2021a). More importantly, the $^{87}Sr/^{86}Sr$ values of the weathering products (0.70496–0.70761) suggest mixing between bedrock and seawater, and the deeper samples also show signals of the marine aerosol end-member (Fig.3b; Fig. 6b). Both the $\tau_{Li}$ and $\delta^7$Li values show that rainwater Li was leached downward and outward from the profile (Brantley and Lebedeva, 2011).

In summary, the external-Li was mainly derived from marine aerosol deposition via rainfall, most of which being leached to the deeper layer or away from the profile under extreme tropical weathering. Similar phenomenon was reported in the Hawaiian basalt weathering profile (Chadwick et al., 2009). The mass fraction of the marine aerosol-derived Sr ($f^{Sr}_{seawater}$) can be calculated with the formula by Stewart et al. (1998):

$$f^{Sr}_{Seawater} = \frac{(^{87}Sr/^{86}Sr)_{soil} - (^{87}Sr/^{86}Sr)_{basalt}}{(^{87}Sr/^{86}Sr)_{seawater} - (^{87}Sr/^{86}Sr)_{basalt}} \times 100\% \quad (4)$$

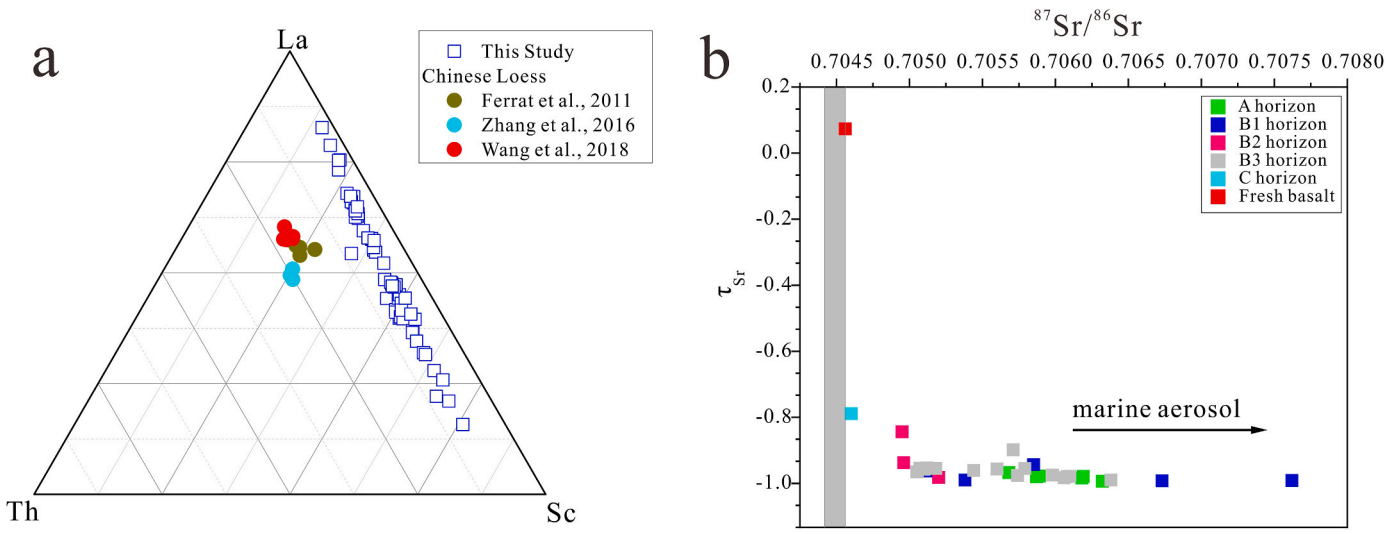


**Fig. 6.** (a) Ternary La–Th-Sc discrimination diagram that compares the Wenchang basalt weathering products with the Chinese loess (Ferrat et al., 2011; Zhang et al., 2016; Wang et al., 2018); (b) $\tau_{Sr}$ vs.$^{87}Sr/^{86}Sr$ for the weathering products. Vertical grey bar represents the fresh basalt $^{87}Sr/^{86}Sr$ range.

where the $(^{87}Sr/^{86}Sr)_{soil}$, $(^{87}Sr/^{86}Sr)_{basalt}$ and $(^{87}Sr/^{86}Sr)_{seawater}$ = $^{87}Sr/^{86}Sr$ values of soil, basalt and seawater, respectively. The calculated $f^{Sr}_{seawater}$ = 9.04–66.12%. As shown in Figs. 3d and 6b, there is an overall negative $^{87}Sr/^{86}Sr$ vs. $\tau_{Sr}$ correlation, indicating major marine aerosol input.

### 5.2. Controls of Li isotope fractionation during extreme basalt weathering

#### 5.2.1. Effect of atmospheric input and secondary mineral dissolution

The Li contents of the samples at the top-level (A-horizon) of the Wenchang profile are lower and exhibit a downward increasing trend, while their $\delta^7$Li values have an upward increasing trend. This phenomenon is similar to that of the Hawaiian basalt weathering profile (with similar rainfall and age; Huh et al., 2004; Ryu et al., 2014) and the diabase weathering profile in South Carolina (Rudnick et al., 2004). The Li elemental/isotope variation trends of our samples, however, are different from those of the top-level samples in some basalt weathering profiles in Hawaii and Columbia (Li et al., 2020; Liu et al., 2013) and andesite weathering profile in Guadeloupe (Clergue et al., 2015), in which both the Li content and $\delta^7$Li value increase upward. Pogge von Strandmann et al. (2021) noticed no clear trends with depth for the soil Li content (or $\delta^7$Li) of the soil profiles in Iceland. Huh et al. (2004) explained the downward Li increasing trend and upward $\delta^7$Li increasing trend by the leaching of marine aerosol Li under heavy rainfall conditions, whilst Ryu et al. (2014) considered that the external input is likely small, and the upward $\delta^7$Li increasing trend for the top-level samples may be due to the preferential leaching of the lighter $^6$Li in secondary mineral dissolution. Rudnick et al. (2004) considered that this phenomenon is difficult to explain and the variation trend is enigmatic.

For the Wenchang basalt weathering profile, the soil samples in A-horizon are mainly composed of kaolinite (halloysite), gibbsite, goethite and hematite, and the distribution of $\tau_{Al}$, $\tau_{Fe}$ and $\tau_{Si}$ in these top-level samples reflects the dissolution and leaching of secondary minerals (Fig. 2d, f, 2g) (Gong et al., 2019). Similar phenomenon was found in Puerto Rico andesitic weathering profile (Chapela Lara et al., 2022), which shows secondary mineral dissolution happened under the intense weathering of the humid tropics. In addition, these top-level samples have low pH (Fig. 2j), and previous studies have shown that Li desorption occurs in aluminosilicate minerals under acidic conditions (Pogge von Strandmann et al., 2012; Clergue et al., 2015). Although the total organic matter (TOC) contents in A-horizon samples are much higher than those in the profile bottom, the Li concentration in the organic matter is very low, and would not cause major Li isotope fractionation in the soil (Lemarchand et al., 2010; Clergue et al., 2015). Li et al. (2020) has shown that $\delta^7$Li of the organic matter fraction is lower than that of the bulk sample, and that organic matter addition would decrease the $\delta^7$Li of the top-level samples. This is inconsistent with the observed upward-increasing $\delta^7$Li trend in A-horizon of the Wenchang profile. Considering also the high $^{87}Sr/^{86}Sr$ and its down-depth increasing trend in the A-horizon samples, we suggest that the Li content and Li isotope behavior at the profile top may be co-influenced by the (1) input and downward migration of marine aerosol, and (2) preferential downward leaching of light Li isotopes, caused by the secondary mineral dissolution under extreme weathering conditions. With the dissolution of secondary mineral, the porewater would be enriched with $^6$Li and move downwards through the regolith (Chapela Lara et al., 2022), this, together with the input of isotopically heavy marine aerosol, producing an upward increasing trend of $\delta^7$Li values at the top of the profile (A horizon).

#### 5.2.2. Fe–Mn oxides-controlled Li enrichment in the profile

As a monovalent element, lithium distribution is generally considered to be redox-insensitive (Penniston-Dorland et al., 2017). However, lithium can be adsorbed on secondary minerals (e.g., Fe–Mn oxides), and is thus indirectly controlled by the redox state (Zhang et al., 2021b). Previous studies have shown that Fe–Mn oxides in river sediments and weathered soils can host (by adsorption) a large amount of lithium, preferentially $^6$Li (Chan and Hein, 2007; Millot et al., 2010b; Négrel and Millot, 2019; Zhang et al., 2021b).

For the Wenchang weathering profile, we noticed that: (1) XRD and SEM-EDS mineralogical analyses show that secondary carbonates, quartz and gypsum are present in the middle part of the profile, indicating weak leaching or unsaturated soil solution, and that these minerals are most likely formed in alternating dry and wet seasons (Jiang et al., 2018); (2) The Rb/Sr ratio correlate positively with the intensity of weathering and leaching (Chen et al., 1999), while $\tau_{Fe}$ and Ce/Ce* may reflect the leaching of redox-sensitive elements Fe and Ce under oxidizing conditions (Ma et al., 2007). Both $\tau_{Fe}$ (Fig. 2d), Ce/Ce* (Fig. 2e) and Rb/Sr ratios (Fig. 3c) of samples show similar peaks at the upper and bottom, and a depletion in the middle part of B1-horizon, indicating that these samples have experienced multiple leaching and desorption processes; (3) Sequential extraction results indicate that Li occurs mainly in the Fe–Mn oxide fraction of B1 samples (Fig. 4a). The oscillating $\delta^7$Li distribution along depth in this horizon may be attributed to the multiple Fe–Mn oxide leaching and desorption. The MnO

enrichment in B2-horizon samples indicates that Fe–Mn oxides precipitated at this depth. Mn-rich samples have the highest Li content (or $\tau_{Li}$) and the lowest $\delta^7$Li value (Fig. 2a, b, 2c), indicating that Fe–Mn oxides preferential adsorption $^6$Li. Therefore, we suggest that the Li geochemical behavior in B1- and B2-horizonsis mainly controlled by the dissolution and precipitation of secondary Fe–Mn oxides.

Lithium content of the B3-horizon samples displays a downward-decreasing trend, along which the first-increasing and then decreasing $\delta^7$Li value (Fig. 2a–b). The sequential extraction experiment results show that Li exists mainly in the residue in these samples. As above-mentioned, large amount of $^6$Li in the B2-horizon is adsorbed on Fe–Mn oxides, which drives higher the $\delta^7$Li value of pore-water, from which secondary minerals are then precipitating (Pogge von Strandmann et al., 2021). This can explain the increasing $\delta^7$Li trend in the upper B3-horizon (7.10–9.84 m) samples and the heaviest saprolite $\delta^7$Li (up to 8.9‰) at 9.84 m depth. Below this depth, there is a negative $\tau_{Li}$ vs. $\delta^7$Li correlation in the lower B3-horizon (9.84–15.28 m) samples (Fig. 7a). This indicates that as Li is percolating downward, the pore-water $\delta^7$Li tends to be lower, which is inherited by the newly-formed secondary minerals (Tong et al., 2021; Chapela Lara et al., 2022). In addition, $\delta^7$Li correlates negatively with pH in these samples (Fig. 7b), indicating that pH can promote the Li adsorption on secondary minerals with depth, forming the low-$\delta^7$Li weathering products (Li et al., 2020).

### 5.2.3. *Initial weathering of basalts and Li enrichment at rock-regolith interface*

The semi-weathered basalt (C-horizon) sample at the rock-regolith interface shows Li enrichment ($\tau_{Li}$ = up to 4.3), but its $\delta^7$Li value does not change significantly (−2.68‰, close to the fresh basalt value). This may be related to the mineral composition and low weathering intensity (CIA = 69.1%; Table 1; Fig. 2h) in this horizon, and the latter would reduce the Li loss. Moreover, the continuous leaching/downward-percolation of soil solution can also lead to the Li enrichment. The semi-weathered basalt sample still contains some residual primary minerals (plagioclase, pyroxene) and early-stage weathering minerals, such as montmorillonite and chlorite (Jiang et al., 2018). Lithium isotopes do not fractionate during the partial dissolution of basalts or primary mineral dissolution (Pistiner and Henderson, 2003; Ryu et al., 2014). Moreover, owing to lower weathering intensity, secondary minerals scavenged some $^6$Li, which shifts the $\delta^7$Li of the semi-weathered sample toward that of the bedrock.

## 5.3. *Implications*

Chemical weathering of basalts can significantly change the bedrock chemical composition by leaching the more mobile elements out of the profile. The Wenchang basalt profile is highly weathered (CIA ~100%), and alkalis (Na, K, and Ca) are mostly lost. Under strong leaching, the Sr–Li input from ocean aerosol can affect the entire profile, and secondary minerals have undergone multiple adsorption and desorption processes (forming the wide $\delta^7$Li range). Owing to the secondary mineral dissolution and Fe–Mn oxide adsorption, some saprolite samples in B3-horizon have higher $\delta^7$Li values than the bedrock, which implies that the corresponding $\delta^7$Li value of the soil solution would be relatively low (Tong et al., 2021; Chapela Lara et al., 2022). Our results support the non-linear correlation between dissolved $\delta^7$Li and the weathering intensity (both high and low weathering intensity produce low dissolved $\delta^7$Li values, but at very different Li fluxes) (Dellinger et al., 2015; Pogge von Strandmann et al., 2020).

Compared with other basalt or andesite weathering profiles (Huh et al., 2004; Kisakürek et al., 2004; Pogge von Strandmann et al., 2012; Liu et al., 2013; Ryu et al., 2014; Clergue et al., 2015; Li et al., 2020; Tong et al., 2021; Chapela Lara et al., 2022), the Li elemental and isotopic compositions of the Wenchang samples vary greatly, and the Li content of most samples is lower than those of other profiles (Fig. 8). Except for a few samples from the Hawaiian weathering profile (which

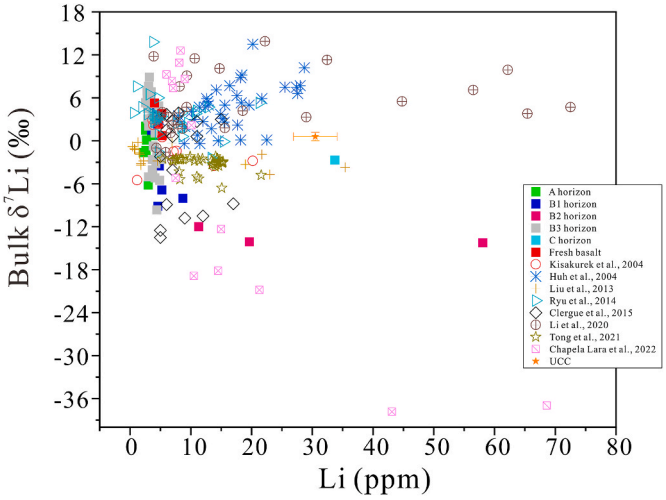


**Fig. 8.** $\delta^7$Li vs. Li content plot for the Wenchang basalt weathering products and other basalt-andesite weathering profiles (Huh et al., 2004; Kisakürek et al., 2004; Liu et al., 2013; Pogge von Strandmann et al., 2012; Ryu et al., 2014; Clergue et al., 2015; Li et al., 2020; Tong et al., 2021; Chapela Lara et al., 2022); UCC: upper continental crust (Sauzéat et al., 2015).

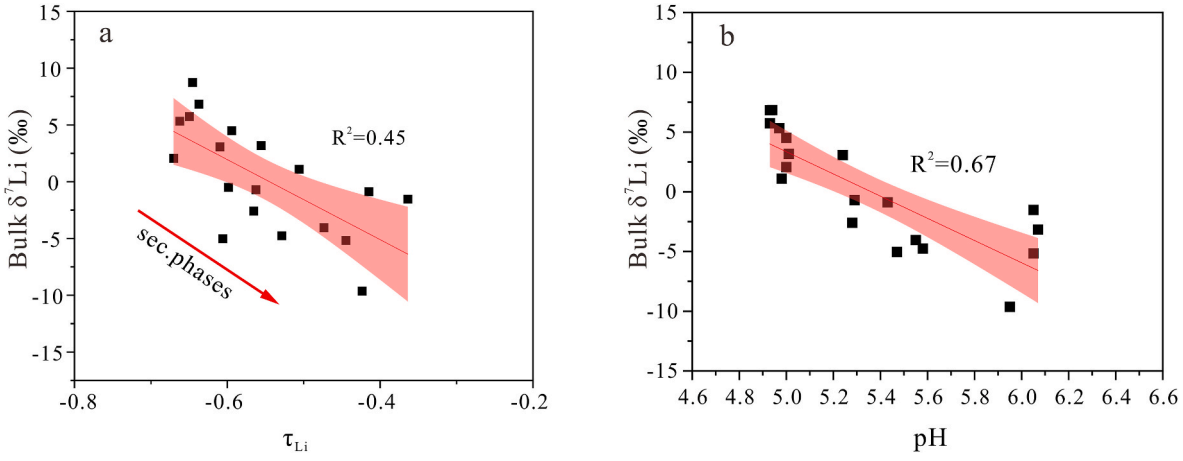


**Fig. 7.** Bulk $\delta^7$Li vs. (a) $\tau_{Li}$ and (b) pH of B3-horizon samples (WC-34 to WC-52) from the Wenchang basalt weathering profile.

are affected by biological and atmospheric input) (Li et al., 2020), and the Puerto Rico andesite weathering profile (the lowest $\delta^7$Li value is low as −37.83‰, resulting by the dissolution of secondary clay minerals and secondary mineral precipitation; Chapela Lara et al., 2022), the Wenchang B2-horizon samples have higher Li content and lower $\delta^7$Li value. For those samples with high Fe–Mn oxide content, the Li content is up to ten times of the bedrock. Fe–Mn oxides are major non-residual oxides in soil and rivers, and have strong adsorption capacity for many elements, such as Cu, Zn, Ni, Pb, Ba (Carpenter et al., 1975; Little et al., 2019; Gong et al., 2020). As illustrated by this study, the Li adsorption on Fe–Mn oxides may be important to the Li enrichment in the red soil weathering profile (Pistiner and Henderson, 2003; Chan and Hein, 2007; Millot et al., 2010b; Wimpenny et al., 2010b).

## 6. Conclusions

We investigated the Li elemental and isotopic behaviors during extreme weathering of basalts from the Hainan Island, South China. Lithium content of most samples is lower than that of fresh basalts, but two distinct peaks are present in the middle section and the rock-saprolite interface. The $\delta^7$Li values vary widely and have complex fluctuations with depth. Strontium isotope evidence indicates that the external-Li was mainly marine aerosol-derived, most of which being leached to deeper-level or out of the profile. Under such extreme weathering conditions, the Li of the upper-section samples may have been desorbed and leached downward, and re-concentrated in the middle-section of the profile. Sequential extraction results indicate that Li occurs mainly in Fe–Mn oxide fraction, Mn-rich samples have the highest Li content (or $\tau_{Li}$) and lowest $\delta^7$Li value, suggesting that such enrichment is controlled by Fe–Mn oxides. In the lower section of the profile, the saprolite Li isotope composition is mainly controlled by high-$\delta^7$Li secondary minerals and pore water. Our study highlights the importance of marine aerosol input to the profile. In addition to the adsorption and desorption of secondary minerals, Fe–Mn oxides may also retain large amount of lithium and lead to significant Li isotope fractionation ($^6$Li enrichment) in the extreme basalt weathering profiles.

## Credit author statement

Hua-Wen Qi: Funding, project design, and supervision. Yan-Wen Xiong: Investigation and manuscript writing. Rui-Zhong Hu: Data interpretation and discussion. Yi-Lin Xiao: Lithium isotope analysis. Li-Yan Wei: Data interpretation and discussion.

## Declaration of competing interest

The authors declare that they have no known competing financial interests or personal relationships that could have appeared to influence the work reported in this paper.

## Acknowledgments

This research was financially supported by the National Natural Science Foundation of China (41673052). We thank Dr. Feng-Tai Tong (USTC) for helping with the MC-ICP-MS analyses. The authors appreciate the constructive comments and suggestions of Pogge von Strandmann and an anonymous reviewer, which significantly improved the quality of data interpretation of the manuscript. Language editing service by Cenozoic Editing & Consultancy (Australia) is acknowledged.

## Appendix A. Supplementary data

Supplementary data to this article can be found online at https://doi.org/10.1016/j.apgeochem.2022.105295.

## References

Berner, R.A., Lasaga, A.C., Garrels, R.M., 1983. The carbonate-silicate geochemical cycle and its effect on atmospheric carbon dioxide over the past 100 million years. Am. J. Sci. 283, 641–683. https://doi.org/10.2475/ajs.283.7.641.

Biscaye, P.E., Grousset, F.E., Revel, M., Gaast, S., Zielinski, G.A., Vaars, A., Kukla, G., 1997. Asian provenance of glacial dust (stage 2) in the Greenland ice sheet project 2 ice core, summit, Greenland. J. Geophys. Res.: Oceans 102, 26765–26781. https://doi.org/10.1029/97JC01249.

Bohlin, M.S., Bickle, M.J., 2019. The reactive transport of Li as a monitor of weathering processes in kinetically limited weathering regimes. Earth Planet Sci. Lett. 511, 233–243. https://doi.org/10.1016/j.epsl.2019.01.034.

Brantley, S.L., Lebedeva, M., 2011. Learning to read the chemistry of regolith to understand the critical zone. Annu. Rev. Earth Planet Sci. 39, 387–416. https://doi.org/10.1146/annurev-earth-040809-152321.

Brimhall, G.H., Dietrich, W.E., 1987. Constitutive mass balance relations between chemical composition, volume, density, porosity, and strain in metasomatic hydrochemical systems: results on weathering and pedogenesis. Geochem. Cosmochim. Acta 51, 567–587. https://doi.org/10.1016/0016-7037(87)90070-6.

Carpenter, R.H., Pope, T.A., Smith, R.L., 1975. Fe-Mn oxide coatings in stream sediment geochemical surveys. J. Geochem. Explor. 4, 349–363. https://doi.org/10.1016/0375-6742(75)90015-1.

Chadwick, O.A., Brimhall, G.H., Hendricks, D.M., 1990. From a black to a gray box—a mass balance interpretation of pedogenesis. Geomorphology 3, 369–390. https://doi.org/10.1016/0169-555X(90)90012-F.

Chadwick, O.A., Derry, L.A., Bern, C.R., Vitousek, P.M., 2009. Changing sources of strontium to soils and ecosystems across the Hawaiian Islands. Chem. Gol. 267, 64–76. https://doi.org/10.1016/j.chemgeo.2009.01.009.

Chan, L.H., Hein, J.R., 2007. Lithium contents and isotopic compositions of ferromanganese deposits from the global ocean. Deep Sea Res., Part II 54, 1147–1162. https://doi.org/10.1016/j.dsr2.2007.04.003.

Chapela Lara, M., Buss, H.L., Henehan, M.J., Schuessler, J.A., McDowell, W.H., 2022. Secondary minerals drive extreme lithium isotope fractionation during tropical weathering. J. Geophys. Res.: Earth Surf. 127, e2021JF006366 https://doi.org/10.1029/2021JF006366.

Chen, J., Wang, Y.J., Ji, J.F., Chen, Y., Lu, H.Y., 1999. Rb/Sr variations and its climatic stratigraphical significance of a loess-paleosol profile from Luochuan, Shaanxi Province. Quat. Sci. 19, 350–356.

Clergue, C., Dellinger, M., Buss, H.L., Gaillardet, J., Benedetti, M.F., Dessert, C., 2015. Influence of atmospheric deposits and secondary minerals on Li isotopes budget in a highly weathered catchment, Guadeloupe (Lesser Antilles). Chem. Geol. 414, 28–41. https://doi.org/10.1016/j.chemgeo.2015.08.015.

Cuong, D.T., Obbard, J.P., 2006. Metal speciation in coastal marine sediments from Singapore using a modified BCR-sequential extraction procedure. Appl. Geochem. 21, 1335–1346. https://doi.org/10.1016/j.apgeochem.2006.05.001.

Dauphas, N., John, S.G., Rouxel, O., 2017. Iron isotope systematics. Rev. Mineral. Geochem. 82, 415–510. https://doi.org/10.2138/rmg.2017.82.11.

Dellinger, M., Gaillardet, J., Bouchez, J., Calmels, D., Louvat, P., Dosseto, A., Gorge, C., Alanoca, L., Maurice, L., 2015. Riverine Li isotope fractionation in the Amazon River basin controlled by the weathering regimes. Geochem. Cosmochim. Acta 164, 71–93. https://doi.org/10.1016/j.gca.2015.04.042.

Dessert, C., Dupré, B., Gaillardet, J., François, L.M., Allègre, C.J., 2003. Basalt weathering laws and the impact of basalt weathering on the global carbon cycle. Chem. Geol. 202, 257–273. https://doi.org/10.1016/j.chemgeo.2002.10.001.

Elliott, T., Steele, R.C.J., 2017. The isotope geochemistry of Ni. Rev. Mineral. Geochem. 82, 511–542. https://doi.org/10.2138/rmg.2017.82.12.

Ferrat, M., Weiss, D.J., Strekopytov, S., Dong, S.F., Chen, H.C., Najorka, J., Sun, Y.B., Gupta, S., Tada, R., Sinha, R., 2011. Improved provenance tracing of Asian dust sources using rare earth elements and selected trace elements for palaeomonsoon studies on the eastern Tibetan Plateau. Geochem. Cosmochim. Acta 75, 6374–6399. https://doi.org/10.1016/j.gca.2011.08.025.

Gaillardet, J., Dupré, B., Louvat, P., Allègre, C.J., 1999. Global silicate weathering and $CO_2$ consumption rates deduced from the chemistry of large rivers. Chem. Geol. 159, 3–30. https://doi.org/10.1016/S0009-2541(99)00031-5.

Gao, Y.J., Casey, J.F., 2012. Lithium isotope composition of ultramafic geological reference materials JP-1 and DTS-2. Geostand. Geoanal. Res. 36, 75–81. https://doi.org/10.1111/j.1751-908X.2011.00117.x.

Gardner, L.R., Kheoruenromne, I., Chen, H.S., 1981. Geochemistry and mineralogy of an unusual diabase saprolite near Columbia, South Carolina. Clay Clay Miner. 29, 184–190. https://doi.org/10.1346/CCMN.1981.0290303.

Gong, Y.Z., Zeng, Z., Chen, Z., Nan, X.Y., Yu, H.M., Lu, Ying, Li, W.Y., Gou, W.X., Cheng, W.H., Huang, F., 2019. Barium isotopic fractionation in latosol developed from strongly weathered basalt. Sci. Total Environ. 687, 1295–1304. https://doi.org/10.1016/j.scitotenv.2019.05.427.

Gong, Y.Z., Zeng, Z., Cheng, W.H., Lu, Y., Zhang, L.L., Yu, H.M., Huang, F., 2020. Barium isotopic fractionation during strong weathering of basalt in a tropical climate. Environ. Int. 143, 105896. https://doi.org/10.1016/j.envint.2020.105896.

Gou, L.F., Jin, Z.D., Pogge von Strandmann, P.A., Li, G., Qu, Y.X., Xiao, J., Deng, L., Galy, A., 2019. Li isotopes in the middle Yellow River: seasonal variability, sources and fractionation. Geochem. Cosmochim. Acta 248, 88–108. https://doi.org/10.1016/j.gca.2019.01.007.

He, M.Y., Dong, J.B., Jin, Z.D., Liu, C.Y., Xiao, J., Zhang, F., Sun, H., Zhao, Z.Q., Gou, L. F., Liu, W.G., Luo, C.G., Song, Y.G., Ma, L., Deng, L., 2021. Pedogenic processes in loess-paleosol sediments: clues from Li isotopes of leachate in Luochuan loess. Geochem. Cosmochim. Acta 299, 151–162. https://doi.org/10.1016/j.gca.2021.02.021.

Hindshaw, R.S., Tosca, R., Goût, T.L., Farnan, I., Tosca, N.J., Tipper, E.T., 2019. Experimental constraints on Li isotope fractionation during clay formation. Geochem. Cosmochim. Acta 250, 219–237. https://doi.org/10.1016/j.gca.2019.02.015.

Hofmann, A.E., Bourg, I.C., DePaolo, D.J., 2012. Ion desolvation as a mechanism for kinetic isotope fractionation in aqueous systems. Proc. Natl. Acad. Sci. Unit. States Am. 109, 18689–18694. https://doi.org/10.1073/pnas.1208184109.

Huh, Y., Chan, L.H., Chadwick, O.A., 2004. Behavior of lithium and its isotopes during weathering of Hawaiian basalt. G-cubed 5, 1–22. https://doi.org/10.1029/2004GC000729.

Jeffcoate, A.B., Elliott, T., Thomas, A., Bouman, C., 2004. Precise, small sample size determinations of lithium isotopic compositions of geological reference materials and modern seawater by MC-ICP-MS. Geostand. Geoanal. Res. 28, 161–172. https://doi.org/10.1111/j.1751-908X.2004.tb01053.x.

Jiang, K., Qi, H.W., Hu, R.Z., 2018. Element mobilization and redistribution under extreme tropical weathering of basalts from the Hainan Island, South China. J. Asian Earth Sci. 158, 80–102. https://doi.org/10.1016/j.jseaes.2018.02.008.

Kisakürek, B., Widdowson, M., James, R.H., 2004. Behaviour of Li isotopes during continental weathering: the Bidar laterite profile, India. Chem. Geol. 212, 27–44. https://doi.org/10.1016/j.chemgeo.2004.08.027.

Kısakűrek, B., James, R.H., Harris, N.B.W., 2005. Li and δ7Li in Himalayan rivers: proxies for silicate weathering? Earth Planet Sci. Lett. 237, 387–401. https://doi.org/10.1016/j.epsl.2005.07.019.

Kurtz, A., Derry, L.A., Chadwick, O.A., Alfano, M.J., 2000. Refractory element mobility in volcanic soils. Geology 28, 683–686. https://doi.org/10.1130/0091-7613(2000)28%3C683:REMIVS%3E2.0.CO, 2.

Lemarchand, E., Chabaux, F., Vigier, N., Millot, R., Pierret, M.C., 2010. Lithium isotope systematics in a forested granitic catchment (Strengbach, Vosges Mountains, France). Geochem. Cosmochim. Acta 74, 4612–4628. https://doi.org/10.1016/j.gca.2010.04.057.

Li, J.W., Zhang, G.L., Ruan, L., Yang, J.L., Wang, H.L., 2016. Sr–Nd elements and isotopes as tracers of dust input in a tropical soil chronosequence. Geoderma 262, 227–234. https://doi.org/10.1016/j.geoderma.2015.08.007.

Li, W.S., Liu, X.M., 2020. Experimental investigation of lithium isotope fractionation during kaolinite adsorption: implications for chemical weathering. Geochem. Cosmochim. Acta 284, 156–172. https://doi.org/10.1016/j.gca.2020.06.025.

Li, W.S., Liu, X.M., Chadwick, O.A., 2020. Lithium isotope behavior in Hawaiian regoliths: soil-atmosphere-biosphere exchanges. Geochem. Cosmochim. Acta 285, 175–192. https://doi.org/10.1016/j.gca.2020.07.012.

Little, S.H., et al., 2019. Cu and Zn isotope fractionation during extreme chemical weathering. Geochem. Cosmochim. Acta 263, 85–107. https://doi.org/10.1016/j.gca.2019.07.057.

Liu, J.Q., Ren, Z.Y., Nichols, A.R.L., Song, M.S., Qian, S.P., Zhang, Y., Zhao, P.P., 2015. Petrogenesis of late Cenozoic basalts from north Hainan Island: constraints from melt inclusions and their host olivines. Geochem. Cosmochim. Acta 152, 89–121. https://doi.org/10.1016/j.gca.2014.12.023.

Liu, X.M., Rudnick, R.L., McDonough, W.F., Cummings, M.L., 2013. Influence of chemical weathering on the composition of the continental crust: insights from Li and Nd isotopes in bauxite profiles developed on Columbia River Basalts. Geochem. Cosmochim. Acta 115, 73–91. https://doi.org/10.1016/j.gca.2013.03.043.

Ma, J.L., Wei, G.J., Xu, Y.G., Long, W.G., Sun, W.D., 2007. Mobilization and re-distribution of major and trace elements during extreme weathering of basalt in Hainan Island, South China. Geochem. Cosmochim. Acta 71, 3223–3237. https://doi.org/10.1016/j.gca.2007.03.035.

Marschall, H.R., Dorsey Wanless, V., Shimizu, N., Pogge von Strandmann, P.A.E., Elliott, T., Monteleone, B.D., 2017. The boron and lithium isotopic composition of mid-ocean ridge basalts and the mantle. Geochem. Cosmochim. Acta 207, 102–138. https://doi.org/10.1016/j.gca.2017.03.028.

McLennan, S.M., 1993. Weathering and global denudation. J. Geol. 101, 295–303. https://doi.org/10.1086/648222.

Millot, R., Petelet-Giraud, E., Guerrot, C., Négrel, P., 2010a. Multi-isotopic composition ($\delta^7$Li–$\delta^{11}$B–δD–$\delta^{18}$O) of rainwaters in France: origin and spatio-temporal characterization. Appl. Geochem. 25, 1510–1524. https://doi.org/10.1016/j.apgeochem.2010.08.002.

Millot, R., Vigier, N., Gaillardet, J., 2010b. Behaviour of lithium and its isotopes during weathering in the Mackenzie Basin, Canada. Geochem. Cosmochim. Acta 74, 3897–3912. https://doi.org/10.1016/j.gca.2010.04.025.

Misra, S., Froelich, P.N., 2012. Lithium isotope history of Cenozoic seawater: changes in silicate weathering and reverse weathering. Science 335, 818–823. https://doi.org/10.1126/science.1214697.

Moynier, F., Vance, D., Fujii, T., Savage, P., 2017. The isotope geochemistry of zinc and copper. Rev. Mineral. Geochem. 82, 543–600. https://doi.org/10.2138/rmg.2017.82.13.

Négrel, P., Millot, R., 2019. Behaviour of Li isotopes during regolith formation on granite (Massif Central, France): controls on the dissolved load in water, saprolite, soil and sediment. Chem. Geol. 523, 121–132. https://doi.org/10.1016/j.chemgeo.2019.05.037.

Nesbitt, H.W., 1979. Mobility and fractionation of rare earth elements during weathering of a granodiorite. Nature 279, 206–210. https://doi.org/10.1038/279206a0.

Nesbitt, H.W., Markovics, G., Price, R.C., 1980. Chemical processes affecting alkalis and alkaline earths during continental weathering. Geochem. Cosmochim. Acta 44, 1659–1666. https://doi.org/10.1016/0016-7037(80)90218-5.

Nesbitt, H.W., Young, G.M., 1982. Early Proterozoic climates and plate motions inferred from major element chemistry of lutites. Nature 299, 715–717. https://doi.org/10.1038/299715a0.

Ollier, C.D., 1988. Deep weathering, groundwater and climate. Geogr. Ann. A. 70, 285–290. https://doi.org/10.1080/04353676.1988.11880258.

Penniston-Dorland, S., Liu, X.-M., Rudnick, R.L., 2017. Lithium isotope geochemistry. Rev. Mineral. Geochem. 82, 165–217. https://doi.org/10.2138/rmg.2017.82.6.

Pistiner, J.S., Henderson, G.M., 2003. Lithium-isotope fractionation during continental weathering processes. Earth Planet Sci. Lett. 214, 327–339. https://doi.org/10.1016/S0012-821X(03)00348-0.

Pogge von Strandmann, P.A.E., Opfergelt, S., Lai, Y.J., Sigfusson, B., Gislason, S.R., Burton, K.W., 2012. Lithium, magnesium and silicon isotope behavior accompanying weathering in a basaltic soil and pore water profile in Iceland. Earth Planet Sci. Lett. 11–23. https://doi.org/10.1016/j.epsl.2012.05.035, 339–340.

Pogge von Strandmann, P.A.E., Burton, K.W., Opfergelt, S., Eiriksdottir, E.S., Murphy, M.J., Einarsson, A., Gislason, S.R., 2016. The effect of hydrothermal spring weathering processes and primary productivity on lithium isotopes: lake Myvatn, Iceland. Chem. Geol. 445, 4–13. https://doi.org/10.1016/j.chemgeo.2016.02.026.

Pogge von Strandmann, P.A.E., Frings, P.J., Murphy, M.J., 2017. Lithium isotope behaviour during weatheringin the ganges alluvial plain. Geochem. Cosmochim. Acta 198, 17–31. https://doi.org/10.1016/j.gca.2016.11.017.

Pogge von Strandmann, P.A.E., Fraser, W.T., Hammond, S.J., Tarbuck, G., Wood, I.G., Oelkers, E.H., Murphy, M.J., 2019. Experimental determination of Li isotope behaviour during basalt weathering. Chem. Geol. 517, 34–43. https://doi.org/10.1016/j.chemgeo.2019.04.020.

Pogge von Strandmann, P.A.E., Kasemann, S., Wimpenny, J., 2020. Lithium and lithium isotopes in earth's surface cycles. Elements 16, 253–258. https://doi.org/10.2138/gselements.16.4.253.

Pogge von Strandmann, P.A.E., Burton, K.W., Opfergelt, S., Genson, B., Guicharnaud, R.A., Gislason, S.R., 2021. The lithium isotope response to the variable weathering of soils in Iceland. Geochem. Cosmochim. Acta 313, 55–73. https://doi.org/10.1016/j.gca.2021.08.020.

Poitrasson, F., 2017. Silicon isotope geochemistry. Rev. Mineral. Geochem. 82, 289–344. https://doi.org/10.2138/rmg.2017.82.8.

Pueyo, M., Mateu, J., Rigol, A., Vidal, M., Lopez-Sanchez, J.F., Rauret, G., 2008. Use of the modified BCR three-step sequential extraction procedure for the study of trace element dynamics in contaminated soils. Environ. Pollut. 152, 330–341. https://doi.org/10.1016/j.envpol.2007.06.020.

Qi, H.W., Hu, R.Z., Jiang, K., Zhou, T., Liu, Y.F., Xiong, Y.W., 2019. Germanium isotopes and Ge/Si fractionation under extreme tropical weathering of basalts from the Hainan Island, South China. Geochem. Cosmochim. Acta 253, 249–266. https://doi.org/10.1016/j.gca.2019.03.022.

Qin, L.P., Wang, X.L., 2017. Chromium isotope geochemistry. Rev. Mineral. Geochem. 82, 379–414. https://doi.org/10.2138/rmg.2017.82.10.

Rudnick, R.L., Tomascak, P.B., Njo, H.B., Gardner, L.R., 2004. Extreme lithium isotopic fractionation during continental weathering revealed in saprolites from South Carolina. Chem. Geol. 212, 45–57. https://doi.org/10.1016/j.chemgeo.2004.08.008.

Ryu, J.S., Vigier, N., Lee, S.W., Lee, K.S., Chadwick, O.A., 2014. Variation of lithium isotope geochemistry during basalt weathering and secondary mineral transformations in Hawaii. Geochem. Cosmochim. Acta 145, 103–115. https://doi.org/10.1016/j.gca.2014.08.030.

Sauzéat, L., Rudnick, R.L., Chauvel, C., Garçon, M., Tang, M., 2015. New perspectives on the Li isotopic composition of the upper continental crust and its weathering signature. Earth Planet Sci. Lett. 428, 181–192. https://doi.org/10.1016/j.epsl.2015.07.032.

Steinhoefel, G., Brantley, S.L., Fantle, M.S., 2021. Lithium isotopic fractionation during weathering and erosion of shale. Geochem. Cosmochim. Acta 295, 155–177. https://doi.org/10.1016/j.gca.2020.12.006.

Stewart, B.W., Capo, R.C., Chadwick, O.A., 1998. Quantitative strontium isotope models for weathering, pedogenesis and biogeochemical cycling. Geoderma 82, 173–195. https://doi.org/10.1016/S0016-7061(97)00101-8.

Sun, H., Gao, Y., Xiao, Y., Gu, H.O., Casey, J.F., 2016. Lithium isotope fractionation during incongruent melting: constraints from post-collisional leucogranite and residual enclaves from Bengbu Uplift, China. Chem. Geol. 439, 71–82. https://doi.org/10.1016/j.chemgeo.2016.06.004.

Sun, J., 2005. Nd and Sr isotopic variations in Chinese eolian deposits during the past 8 Ma: implications for provenance change. Earth Planet Sci. Lett. 240, 454–466. https://doi.org/10.1016/j.epsl.2005.09.019.

Tasi, P.H., You, C.F., Huang, K.F., Chung, C.H., Sun, Y.B., 2014. Lithium distribution and isotopic fractionation during chemical weathering and soil formation in a loess profile. J. Asian Earth Sci. 87, 80–102. https://doi.org/10.1016/j.jseaes.2014.02.001.

Teng, F.Z., Mcdonough, W.F., Rudnick, R.L., Dalpé, C., Tomascak, P.B., Chappell, B.W., Gao, S., 2004. Lithium isotopic composition and concentration of the upper continental crust. Geochem. Cosmochim. Acta 68, 4167–4178. https://doi.org/10.1016/j.gca.2004.03.031.

Teng, F.Z., Li, W.Y., Rudnick, R.L., Gardner, L.R., 2010. Contrasting lithium and magnesium isotope fractionation during continental weathering. Earth Planet Sci. Lett. 300, 63–71. https://doi.org/10.1016/j.epsl.2010.09.036.

Teng, F.Z., Dauphas, N., Watkins, J.M., 2017. Non-traditional stable isotopes: retrospective and prospective. Rev. Mineral. Geochem. 82, 1–26. https://doi.org/10.2138/rmg.2017.82.1.

Tomascak, P.B., 2004. Developments in the understanding and application of lithium isotopes in the earth and planetary sciences. Rev. Mineral. Geochem. 55, 153–195. https://doi.org/10.2138/gsrmg.55.1.153.

Tong, F.T., Xiao, Y.L., Sun, H., Wang, Y.Y., Wan, H.Q., Gou, L.F., Gong, Y.Z., Huang, F., Li, D.Y., Hou, Z.H., et al., 2021. Lithium isotopic features of Quaternary basaltic

saprolite, Zhanjiang, China: atmospheric input and clay-mineral adsorption. Sci. Total Environ. 785, 147235. https://doi.org/10.1016/j.scitotenv.2021.147235.

Ure, A.M., Quevauviller, P., Muntau, H., Griepink, B., 1993. Speciation of heavy metals in soils and sediments. An account of the improvement and harmonization of extraction techniques undertaken under the auspices of the BCR of the commission of the European communities. Int. J. Environ. Anal. Chem. 51, 135–151. https://doi.org/10.1080/03067319308027619.

Vigier, N., Decarreau, A., Millot, R., Carignan, J., Petit, S., France-Lanord, C., 2008. Quantifying Li isotope fractionation during smectite formation and implications for the Li cycle. Geochem. Cosmochim. Acta 72, 780–792. https://doi.org/10.1016/j.gca.2007.11.011.

Walker, J.C.G., Hays, P.B., Kasting, J.F., 1981. A negative feedback mechanism for the long-term stabilization of Earth's surface temperature. J. Geophys. Res.: Oceans 86. https://doi.org/10.1029/JC086iC10p09776.

Wang, Q.L., Chetelat, B., Zhao, Z.Q., Ding, H., Li, S.L., Wang, B.L., Li, J., Liu, X.L., 2015. Behavior of lithium isotopes in the Changjiang River system: sources effects and response to weathering and erosion. Geochem. Cosmochim. Acta 151, 117–132. https://doi.org/10.1016/j.gca.2014.12.015.

Wang, Z.B., Ma, J.L., Li, J., Wei, G.J., Zeng, T., Li, L., Zhang, L., Deng, W.F., Xie, L.H., Liu, Z.F., 2018. Fe (hydro) oxide controls Mo isotope fractionation during the weathering of granite. Geochem. Cosmochim. Acta 226, 1–17. https://doi.org/10.1016/j.gca.2018.01.032.

Wimpenny, J., Gíslason, S.R., James, R.H., Gannoun, A., Pogge von Strandmann, P.A.E., Burton, K.W., 2010a. The behaviour of Li and Mg isotopes during primary phase dissolution and secondary mineral formation in basalt. Geochem. Cosmochim. Acta 74, 5259–5279. https://doi.org/10.1016/j.gca.2010.06.028.

Wimpenny, J., James, R.H., Burton, K.W., Gannoun, A., Mokadem, F., Gíslason, S.R., 2010b. Glacial effects on weathering processes: new insights from the elemental and lithium isotopic composition of West Greenland rivers. Earth Planet Sci. Lett. 290, 427–437. https://doi.org/10.1016/j.epsl.2009.12.042.

Yang, Y.H., Zhang, H.F., Chu, Z.Y., Xie, L.W., Wu, F.Y., 2010. Combined chemical separation of Lu, Hf, Rb, Sr, Sm and Nd from a single rock digest and precise and accurate isotope determinations of Lu–Hf, Rb–Sr and Sm–Nd isotope systems using Multi-Collector ICP-MS and TIMS. Int. J. Mass Spectrom. 290, 120–126. https://doi.org/10.1016/j.ijms.2009.12.011.

Zhang, J.W., Zhao, Z.Q., Li, X.D., Yan, Y.N., Lang, Y.C., Ding, H., Cui, L.F., Meng, J.L., Liu, C.Q., 2021a. Extremely enrichment of $^{7}$Li in highly weathered saprolites developed on granite from Huizhou, southern China. Appl. Geochem. 125, 104825. https://doi.org/10.1016/j.apgeochem.2020.104825.

Zhang, J.W., Zhao, Z.Q., Yan, Y.N., Cui, L.F., Wang, Q.L., Meng, J.L., Li, X.D., Liu, C.Q., 2021b. Lithium and its isotopes behavior during incipient weathering of granite in the eastern Tibetan Plateau, China. Chem. Geol. 559, 119969. https://doi.org/10.1016/j.chemgeo.2020.119969.

Zhang, W.F., Chen, J., Ji, J.F., Li, G.J., 2016. Evolving flux of asian dust in the north pacific ocean since the late oligocene. Aeoloan Res 23, 11–20. https://doi.org/10.1016/j.aeolia.2016.09.004.

Zhu, Z.Y., Yang, T., Zhu, X.K., 2019. Achieving rapid analysis of Li isotopes in highmatrix and low-Li samples with MC-ICP-MS: new developments in sample preparation and mass bias behavior of Li in ICPMS. J. Anal. At. Spectrom. 34, 1503–1513. https://doi.org/10.1039/C9JA00076C.